Multivariate Image Analysis of Magnetic Resonance Images with the Direct Exponential Curve Resolution Algorithm (DECRA)

Part 2: Application to Human Brain Images

B. Antalek,[1] J. P. Hornak,* and W. Windig

*Imaging Research and Advanced Development, Eastman Kodak Company, Rochester, New York 14650-2132; and *Center for Imaging Science and Department of Chemistry, Rochester Institute of Technology, Rochester, New York 14623-5604*

E-mail: bantalek@kodak.com

Owing to the heterogeneity of living tissues, it is challenging to quantify tissue properties using magnetic resonance imaging. Within a single voxel, contributions to the signal may result from several types of ^1H nuclei with varied chemical (e.g., $-CH_2-$, $-OH$) and physical environments (e.g., tissue density, compartmentalization). Therefore, mixtures of ^1H environments are prevalent. Furthermore, each unique type of ^1H environment may possess a unique and characteristic spin–lattice relaxation time (T_1) and spin–spin relaxation time (T_2). A method for resolving these unique exponentials is introduced in a separate paper (Part 1. Algorithm and Model System) and uses the direct exponential curve resolution algorithm (DECRA). We present results from an analysis of images of the human head comprising brain tissues. © 1998 Academic Press

Key Words: spin relaxation rates; magnetic resonance imaging; MRI; multispectral tissue classification; image segmentation.

INTRODUCTION

Hydrogen NMR spin–lattice and spin–spin relaxation times, T_1 and T_2 respectively, have been used to characterize living tissues (*1–10*). These biological samples are composed of complex spin systems, and several models have been proposed to explain the spin relaxation behavior of such a heterogeneous system (*8*). One model proposes that tissues may be composed of different nonexchanging spin types and therefore possess multiexponential relaxation behavior characteristic of the sum of the individual components. For water alone there have been as many as five different types proposed (*10*). At the opposite extreme is a model proposing that the different spin types are coupled by strong exchange, and hence possess one characteristic T_1 and T_2. In the middle of these two extremes are tissues exhibiting weak exchange and possessing multiexponential relaxation characteristics different from the pure spin components. There is no reason to believe that all tissues behave as one of the three possibilities, or that a given tissue will be spatially homogeneous. Clearly more studies are needed to determine an optimum model for each tissue (*7–9*).

Further complicating these models is the size of the imaged voxel (*6*). Partial volume effects are seen with large voxels that may contain several tissues, each composed of multiple spin environments. It is only at the small-voxel limit that the question of which of the three models is appropriate for a given tissue can be answered. Even if the voxel size approaches the cellular level, we should expect multiexponential relaxation behavior due to the heterogeneity of the living cell anatomy.

Models for such complex systems must be manageable, however. Technical accuracy and practical considerations must be balanced to achieve a robust model. The parameters must be accessible by measurement. A few key components must be identified that describe the vast majority of the data. Other components may exist, but their contributions are within the noise range.

Traditionally, exponential fitting procedures are needed to measure both T_1 and T_2. With all exponential fitting procedures, the resultant relaxation times are only as good as the data being fit. The relationships among signal-to-noise ratio of the data, time interval between points (Δt), shortest time data point t_{min}, longest time data point t_{max}, and calculated exponential time constants have been studied (*11, 12*). For all exponential fits, t_{max} should be at least three times the longest relaxation time. Additionally, for monoexponential
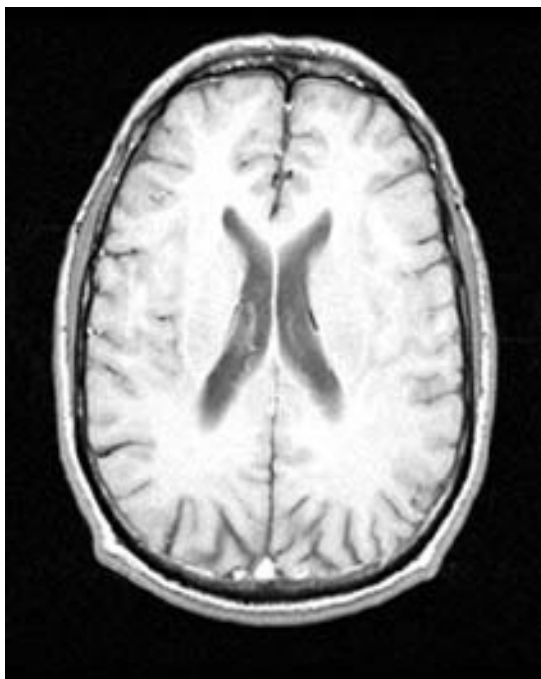
FIG. 1. TR/TE = 1000/15 ms image of the imaged axial slice through the brain.

decays, the first data point should be approximately equal to the shortest relaxation time. For biexponential curves, Δt must be very short, and for multiexponential decay fits the utility is questionable.

Owing to the complexity of the problem, researchers must compromise and take advantage of available techniques in order to gain insight into the relaxation mechanisms in tissues. T_1 and T_2 weighted images of the human body are routinely acquired in clinical MRI (1). These images are easy to obtain, avoid the need for exponential fitting, and provide some insight into the gross variations in the tissue T_1 and T_2 values. Calculated apparent monoexponential T_1 (13) and T_2 (14) images were used to study variations in T_1, T_2, and spin density (ρ) of brain tissues (2). These images can take upwards of an hour to acquire correctly, but clearly demonstrated the partial volume effect on the measured relaxation times. Multiexponential and continuous distributions analyses have been employed and begin to reveal the complexity of the spin system in biological tissues (7–9, 15). These techniques require large amounts of data because of the short Δt requirement that make it time consuming to collect with imaging techniques.

Another image analysis approach involves principal component analysis (PCA). Geladi *et al.* (16–18) and Grahn and Sääf (19) have utilized PCA for analyzing sets of correlated MRI images. This method is fast, does not require a large number of images, and results in a set of extracted images that are based upon principal components. However,

the extracted images are abstract and not strictly related to any real physical parameters such as T_2 or T_1.

In this article, we present a technique that overcomes effects due to spin environment heterogeneity and extracts pure T_1 and T_2 information. We have pursued an approach similar to PCA, which is based upon a procedure developed by Kubista (20, 21) and expressed in terms of the generalized rank annihilation method (GRAM) (22). Kubista's technique was utilized previously by Schulze and Stilbs (23) on a pulsed-gradient spin-echo (PGSE) NMR data set for separating highly overlapped spectra. The experiment, however, required the use of a complicated data acquisition scheme, which compromised the integrity of the spectral bandshapes. Recently, Antalek and Windig (24, 25) utilized the GRAM method on a PGSE NMR data set using a standard data acquisition scheme, which provided good lineshape results and is denoted as DECRA (direct exponential curve resolution algorithm). The algorithm that we use for the image analysis is based upon DECRA. The mathematical procedure for DECRA and examples of the analysis for a phantom are presented elsewhere (25, 26). We report here an example of DECRA applied to magnetic resonance (MR) images of the human head. Because of the nature of the mathematical approach (which models exponential functions), DECRA resolves pure components that are directly related to physically real parameters that describe exponential functions (namely, T_1 and T_2). The pure components are few in number and are regarded as the primary components which describe the vast majority of the image signal distribution. Images that are reconstructed from the resolved components multiplied by their respective proportionality constants are virtually identical to the original images. We provide a simple context based upon nonexchanging ^1H environments with which to describe the signal contribution of the resolved components to the MR images. It is our hope that this paper will stimulate interest in the algorithm applied to MR images. Such studies will further our ability to model the complex spin system of tissues, which will in turn better our understanding of disease.

THEORY

A standard spin-echo imaging sequence (1) is often used to produce images for calculating T_1 and T_2. T_1 is calculated from a series of images with constant echo time, TE, and variable repetition time, TR. T_2 is calculated from a series of images with a constant TR and variable TE. Assuming that the repetition time of a standard spin-echo imaging sequence is much larger than the echo time, the signal from a voxel containing m nonexchanging ^1H types is

$$S = k \sum_m \rho_m e^{-TE/T_{2m}}(1 - e^{-TR/T_{1m}}), \qquad [1]$$
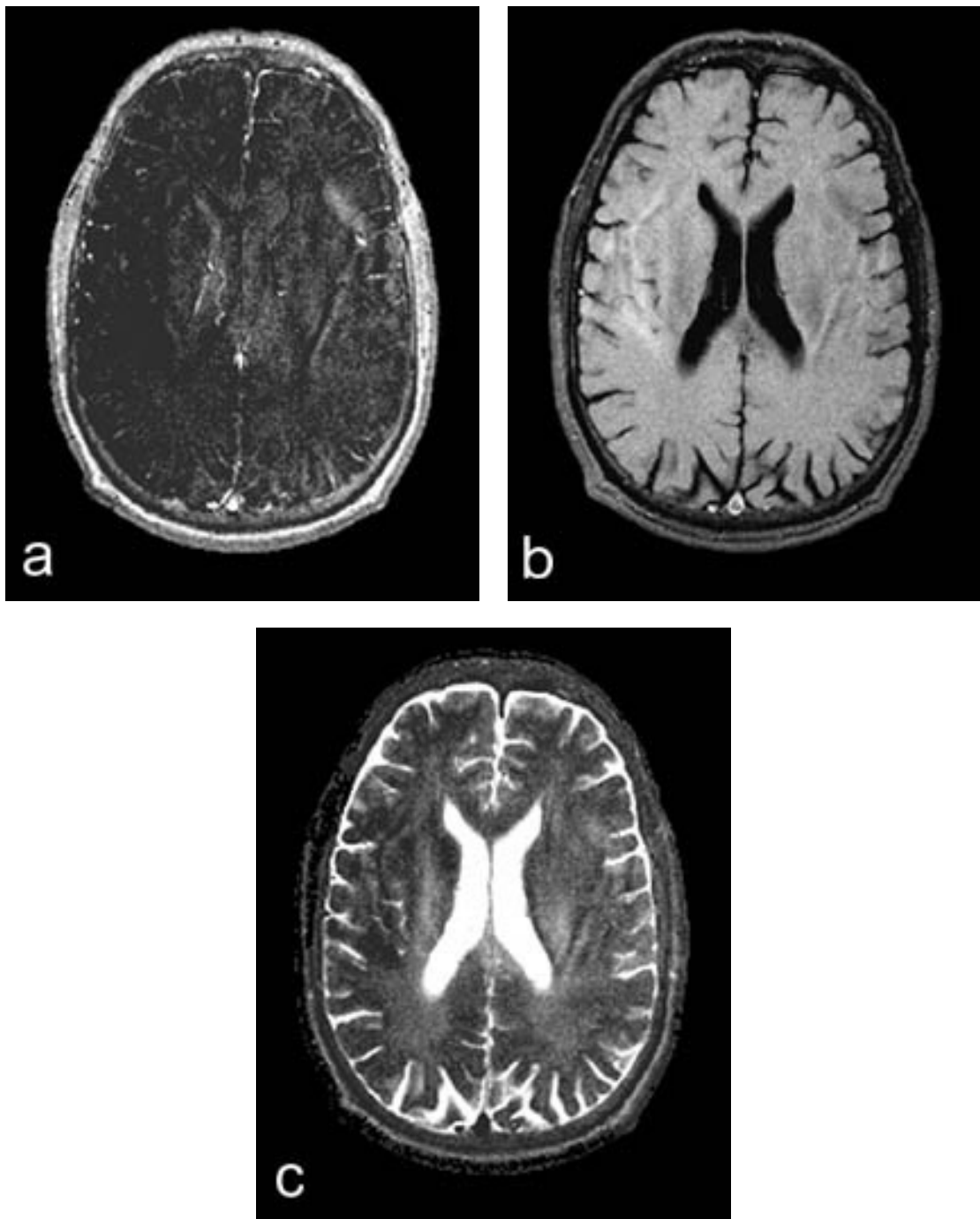
FIG. 2. Resolved component images from DECRA analysis applied to T_2 image series using all 14 images. Component (a) C_1, $T_2 = 22$ ms; (b) C_2, $T_2 = 64$ ms; and (c) C_3, $T_2 = 290$ ms.

where k is a proportionality constant. ρ_m is the spin density of component m in the voxel with T_{1m} and T_{2m}. Since an exponential relationship exists between the signal and the intrinsic sample parameters T_1 and T_2, DECRA may be used to extract images of the unique T_1 and T_2 values. These images are a function of the spin densities and the T_1 and T_2 values. This relationship can best be seen by rewriting Eq. [1] in terms of the i unique T_1 and j unique T_2 values found by DECRA:

$$S = k \sum_i \sum_j \rho_{i,j}(1 - e^{-\text{TR}/T_{1i}})e^{-\text{TE}/T_{2j}}. \qquad [2]$$
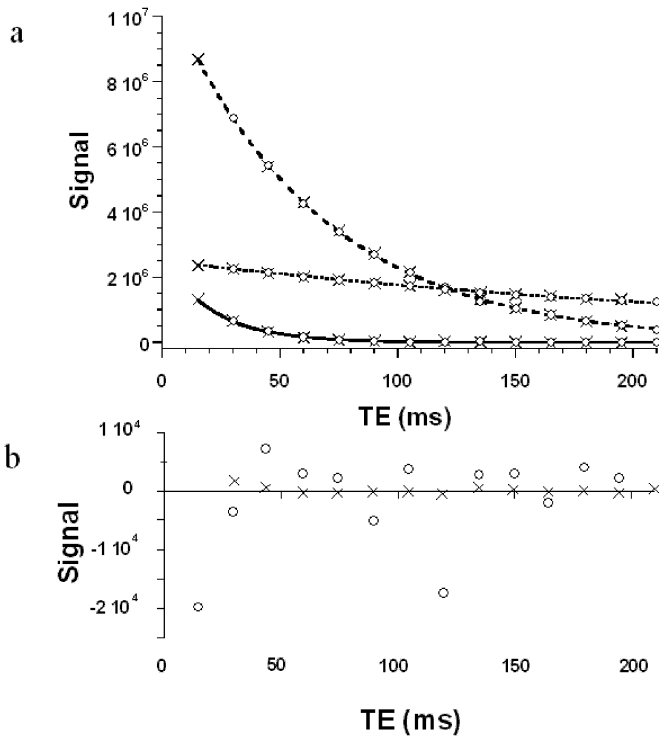
FIG. 3. (a) Exponential contribution profiles calculated from the $T_2 =$ 22 ms (—), 64 ms (- - -), and 290 ms ($\cdot\cdot\cdot$) eigenvalues. The resolved contributions representative of the first part of the split data set (images 1–14) are shown with the $\times$ symbols. The $\bigcirc$ symbols represent the contributions from the second part of the split data set (images 2–15) and are calculated by multiplying the contribution profile of the first data set by its associated eigenvalue calculated by the algorithm. All values have been normalized so that the sum of the three contribution profiles is equal to that of the total signal intensity of the original set of images. (b) Resolved contribution profile for a fourth component showing a noisy structure.

For example, if DECRA finds two T_1 and three T_2 eigenvalues for the image space, there are six possible unique spin components in the image and Eq. [2] becomes

$$S = k[\rho_{1,1}(1 - e^{-\mathrm{TR}/T_{11}})e^{-\mathrm{TE}/T_{21}} + \rho_{1,2}(1 - e^{-\mathrm{TR}/T_{11}})$$
$$\times e^{-\mathrm{TE}/T_{22}} + \rho_{1,3}(1 - e^{-\mathrm{TR}/T_{11}})e^{-\mathrm{TE}/T_{23}}$$
$$+ \rho_{2,1}(1 - e^{-\mathrm{TR}/T_{12}})e^{-\mathrm{TE}/T_{21}} + \rho_{2,2}(1 - e^{-\mathrm{TR}/T_{12}})$$
$$\times e^{-\mathrm{TE}/T_{22}} + \rho_{2,3}(1 - e^{-\mathrm{TR}/T_{12}})e^{-\mathrm{TE}/T_{23}}]. \quad [3]$$

When we collect a T_2 series by keeping TR constant,

$$S = k[(I_1\rho_{1,1} + I_2\rho_{2,1})e^{-\mathrm{TE}/T_{21}} + (I_1\rho_{1,2} + I_2\rho_{2,2})$$
$$\times e^{-\mathrm{TE}/T_{22}} + (I_1\rho_{1,3} + I_2\rho_{2,3})e^{-\mathrm{TE}/T_{23}}], \quad [4]$$

where $I_1 = (1 - e^{-\mathrm{TR}/T_{11}})$ and $I_2 = (1 - e^{-\mathrm{TR}/T_{12}})$. The TE $= 0$ calculated signals from DECRA are $(I_1\rho_{1,1} + I_2\rho_{2,1})$,

$(I_1\rho_{1,2} + I_2\rho_{2,2})$ and $(I_1\rho_{1,3} + I_2\rho_{2,3})$. When we collect a T_1 series by keeping TE constant, Eq. [2] becomes

$$S = k[(J_1\rho_{1,1} + J_2\rho_{1,2} + J_3\rho_{1,3})(1 - e^{-\mathrm{TR}/T_{11}})$$
$$+ (J_1\rho_{2,1} + J_2\rho_{2,2} + J_3\rho_{2,3})(1 - e^{-\mathrm{TR}/T_{12}})], \quad [5]$$

where $J_1 = e^{-\mathrm{TE}/T_{21}}$, $J_2 = e^{-\mathrm{TE}/T_{22}}$, and $J_3 = e^{-\mathrm{TE}/T_{23}}$. The TR $= \infty$ calculated signals are $(J_1\rho_{1,1} + J_2\rho_{1,2} + J_3\rho_{1,3})$ and $(J_1\rho_{2,1} + J_2\rho_{2,2} + J_3\rho_{2,3})$.

Summarizing this example, the image intensity from DECRA yields five components, C, given by Eqs. [6]–[10]:

$$C_1 = (I_1\rho_{1,1} + I_2\rho_{2,1}) \quad [6]$$

$$C_2 = (I_1\rho_{1,2} + I_2\rho_{2,2}) \quad [7]$$

$$C_3 = (I_1\rho_{1,3} + I_2\rho_{2,3}) \quad [8]$$

$$C_4 = (J_1\rho_{1,1} + J_2\rho_{1,2} + J_3\rho_{1,3}) \quad [9]$$

$$C_5 = (J_1\rho_{2,1} + J_2\rho_{2,2} + J_3\rho_{2,3}). \quad [10]$$

In general, the spin densities may not be determined because the number of unknowns exceeds the number of equations. However, in specific cases the spin densities may be determined. For example, if $C_5 = 0$, then ρ_{11}, ρ_{12}, and ρ_{13} may be determined because all ρ, J, and I values must be positive and TR and TE values can be chosen such that J and I are not zero.
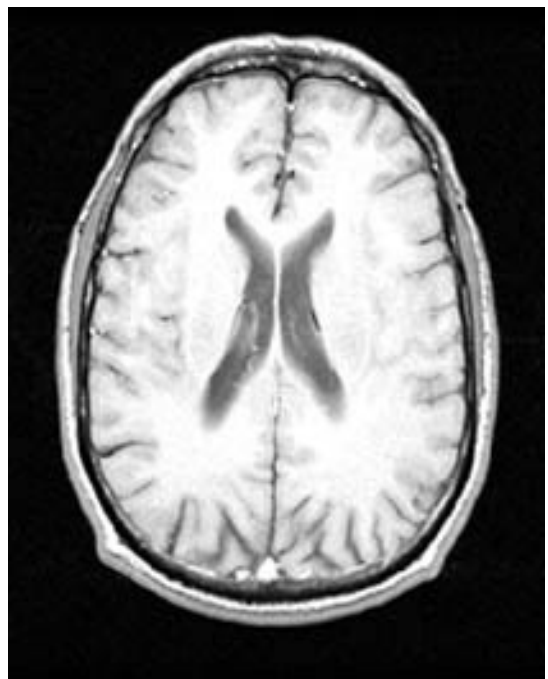
FIG. 4. A TR/TE $= 1000/15$ ms image reconstructed from the three T_2 resolved images of the DECRA analysis. Compare directly with Fig. 1.
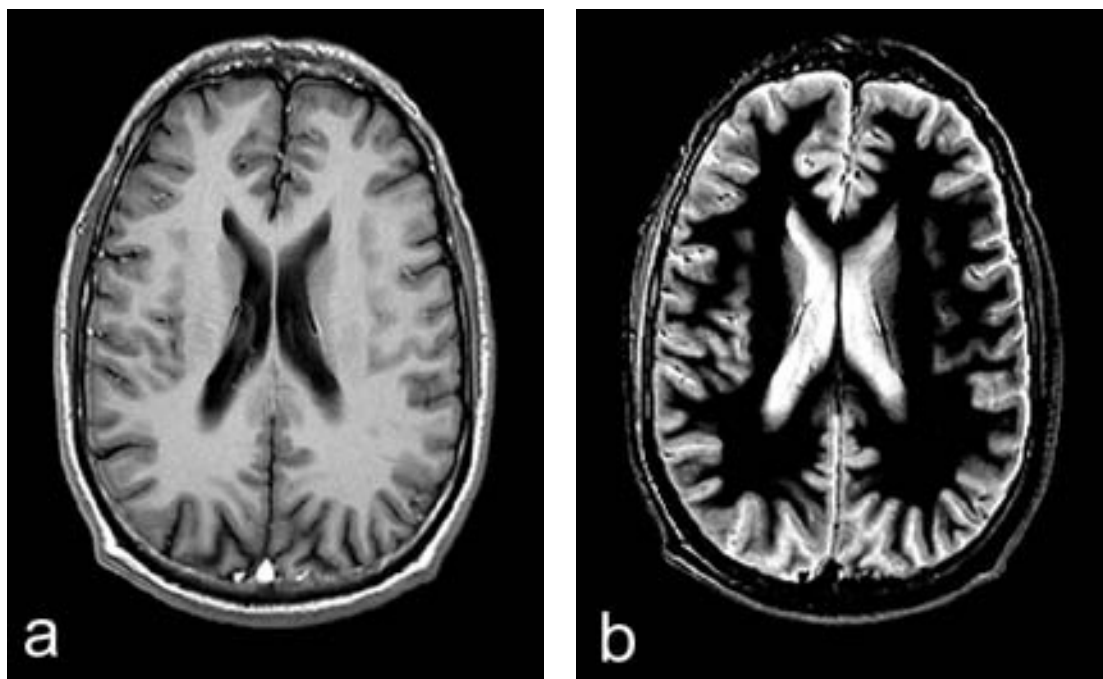
FIG. 5. Resolved component images from DECRA analysis applied to T_1 image series using all 15 images. Component (a) C_4, $T_1 = 0.92$ s; (b) C_5, $T_1 = 7.0$ s.

MATERIALS AND METHODS

A GE Signa (GE Medical Systems, Milwaukee, WI) 1.5-T whole body imager employing a standard single-slice, single-echo, spin-echo pulse sequence and quadrature birdcage-style RF head coil was used to acquire axial magnetic resonance images of the brain. The image plane passed through the head of the age 42 y, healthy male volunteer at the level of the lateral ventricles. (See Fig. 1 for a TR/TE = 1000/15 ms image of the slice location and anatomy.) This slice contained six primary tissue types: cerebral spinal fluid (CSF), gray matter, white matter, meninges, adipose, and muscle. Two sets of images were acquired of this slice: a set used to calculate T_2 in which the echo time (TE) was varied, and a set used to calculate T_1 in which the repetition time (TR) was varied. The T_2 image set consisted of 14 images with a fixed TR = 1000 ms, and a TE which varied between 15 and 210 ms in 15-ms steps. The T_1 image set consisted of 15 images with a fixed TE = 15 ms, and a TR which varied between 200 and 3000 ms in 200-ms steps. Each 24-cm field of view, 5-mm slice thickness image was acquired with 256 phase encoding steps to form a 256×256 pixel image. The motion of the volunteer was found to be minimal during the course of data collection, so no attempt was made to register the pixels within the series of correlated brain images.

The image slice is treated as a mixture of principal T_1 and T_2 components. DECRA was applied to the T_2 and T_1 image sets in order to extract the principal T_2 and T_1 components present, as well as the representative images displaying the relative quantity of each component in a voxel. The 256×256 pixel images were unfolded and processed as a 65,536-element array. Two image sets for each of the image series were organized for input to DECRA. For the T_2 series, the two data sets were the variable TE images 1–13 and 2–14. For the T_1 series, the two data sets were the variable TR images 1–14 and 2–15. As a demonstration of the utility of DECRA on smaller data sets, a T_2 analysis using two alternative data sets, images 1, 4, 7, 10 and 4, 7, 10, 13, was conducted. The DECRA analysis is run using MATLAB (The MathWorks, Inc., Natich, MA) running on a 90-MHz Pentium (Intel Corp., Santa Clara, CA) with 64 MB of memory and takes about 40 s for each image series. The exponential constants T_1 and T_2 are derived from the eigenvalues found from the analysis. More details of the data processing are given elsewhere (25, 26).

RESULTS AND DISCUSSION

The main thrust of this report is to demonstrate a novel processing algorithm that, when applied to a multivariate image data set, will extract unique components in the form of images and their contribution in the original data set. The contribution is based upon an exponential relationship
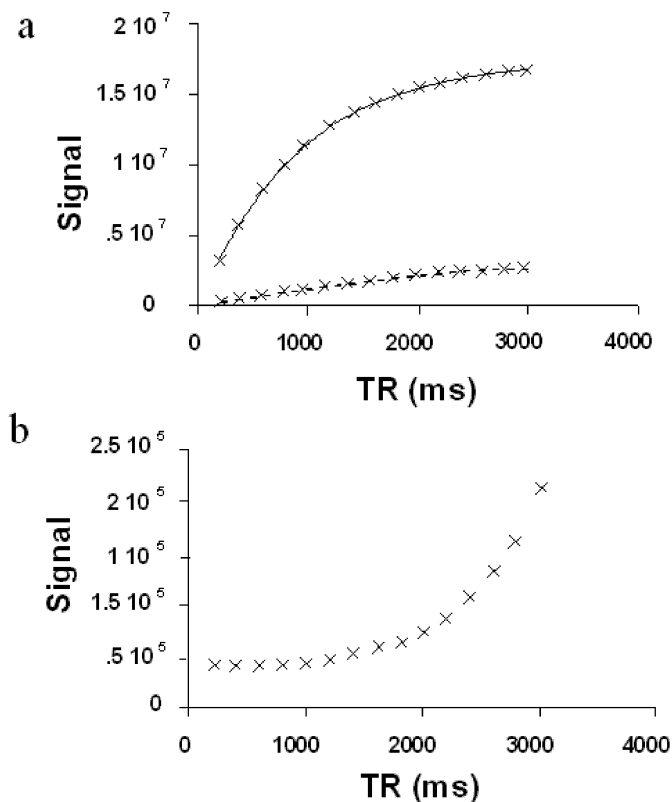
FIG. 6. (a) Resolved contribution profiles of the two components represented in Fig. 5. Components C_4, $T_1 = 0.92$ s (—), and C_5, $T_1 = 7.0$ s (---). (b) The resolved contribution profile for a third component showing an increasing exponential.

between the signal and a known set of acquisition parameters. Hence, a contribution profile is extracted which is exponential in nature. The original data set can be reconstructed from the product of the extracted images and their corresponding signal profiles. We have used both T_1 and T_2 to elucidate the components. In our examples the signal within the resolved (extracted) images are representative of a component having a unique T_1 or T_2 value.

Selecting the number of components is a subjective aspect of the analysis at this time. The choice presents itself clearly, however. There are several criteria to examine when establishing the number of components present in a given data set: (1) the pixel intensities and contribution profiles must be positive; (2) the noise level in the images and contribution profiles should be low; (3) the relative contribution of the component must be significant; and (4) the functional form of the contribution profile needs to fit the model. Generally, a combination of these criteria need to be used.

DECRA was applied to the T_2 image set and three components were found. With each component there is associated both a T_2 value and an image. The three components, referred to as components C_1, C_2, and C_3, have T_2 values of 22, 64, and 290 ms, respectively. Images representing the amount of each component in the signal are presented in Fig. 2. C_1 (Fig. 2a) is found predominantly in meninges, muscle, and adipose tissue. C_2 (Fig. 2b) is present largely in approximately equal amounts in gray and white matter, and to a lesser extent in meninges, muscle, and adipose tissue. C_3 (Fig. 2c) is found extensively in CSF. Although a biological classification is tempting, it is important to realize that the resolved components are defined by a pure exponential decay with its associated T_2 value. Tissue types are complicated mixtures that are composed largely of common building blocks such as intracellular and extracellular water and lipid membranes that can describe the majority of the relaxation behavior. Further work is required to assign the resolved components to a specific material.

The exponential contribution profiles for the three T_2 components are shown in Fig. 3a. The resolved contributions representative of the first (images 1–13) part of the split data set overlaps favorably with that from the second (images 2–14) part of the split data set, calculated by multiplying the contribution profile of the first data set by its associated eigenvalue. This clearly shows that the assumption of proportionality between the points is correct. The lines drawn through the points are calculated directly from the eigenvalues and the normalization factor used for the contribution data. Figure 3b shows the resolved contribution profile for a fourth component (when the data set is analyzed by choosing four components). Obviously, the profile is dominated by noise and does not represent a pure component.

Figure 4 is the first image of the TE series (TR/TE = 1000/15) reconstructed using the component images of C_1, C_2, and C_3 resolved by DECRA. This image can be compared directly with the image in Fig. 1.

DECRA was applied to the T_1 image set and two components, referred to as C_4 and C_5, were found. C_4 had a T_1 of 0.92 s, while C_5 had a T_1 of 7.0 s. It is noted that a T_1 value of 7.0 s appears to be unrealistic (e.g., we should expect a value near 3 s for water at room temperature). However, others (2, 13) have reported long T_1 values in excess of 5 s for CSF using a saturation recovery pulse sequence at a field strength of 1.5 T. They attributed this to a saturation effect arising from the flowing CSF. Images representing the amount of each component in the signal are presented in Fig. 5. C_4 (Fig. 5a) is found in the gray and white brain matter, and in the adipose and muscle tissues. The largest concentration of C_4 appears to be in the adipose tissue. The concentration of C_4 immediately adjacent to the folds in the gray matter is less than in deeper gray matter and white matter of the brain. C_5 (Fig. 5b) is found predominantly in the CSF occupying both the ventricles and the folds in the gray matter. This component also appears to be present in the gray matter adjacent to the folds, but to a lesser concen-

TABLE 1
Tissue Parameters of the Six Hydrogen Environments Found in Imaged Tissues

	T_{1i}, T_{2j} Environment							
i, j	1,1	1,2	1,3	2,1	2,2	2,3		
T_1 (s)	0.92	0.92	0.92	7.0	7.0	7.0		
T_2 (ms)	22	64	290	22	64	290	Monoexponential	
Tissue	$\rho_{1,1}$	$\rho_{1,2}$	$\rho_{1,3}$	$\rho_{2,1}$	$\rho_{2,2}$	$\rho_{2,3}$	T_1 (s)	T_2 (ms)
CSF	0	0	0	0	0	1.0	4.80	425
Gray matter	0	0.5	0	0	0.5	0	1.42	73
White matter	0	0.7	0.3	0	0	0	0.85	73
Muscle	0.35	0.15	0	0.45	0.05	0	1.42	53
Meninges	0.45	0.4	0.15	0	0	0	0.66	48
Adipose	0.45	0.35	0.2	0	0	0	0.34	71

tration than in pure CSF. DECRA did find some of C_5 in the tissues outside of the skull.

The exponential contribution profiles for the two T_1 components are shown in Fig. 6a. For the resolution of the T_1 image series, a transformation of the data set is required (26). This results in correct (for the original data) images but transformed contribution profiles. The exponential contribution profiles of the entire original data set are calculated as the contributions of the resolved images in this data set. As a consequence, we have a single exponential contribution profile for each component instead of two overlapping profiles. The lines drawn through the points are calculated directly from the eigenvalues and the normalization factor used for the contribution data. Figure 6b shows the resolved contribution profile for a third component (when the data set is analyzed by choosing three components). Although the profile is not dominated by noise, as was the case shown in Fig. 3b, it does have a higher noise level than the other two components and has a relative mean value of less than 0.6% of the other two components. The contribution profile is characterized by an increasing exponential which does not fit the model of T_1 relaxation. Furthermore, the resultant image is dominated by noise with equal positive and negative contributions.

The resultant images based upon the DECRA analysis are significantly different from the T_1 or T_2 images obtained through single-exponential fitting routines of registered pixels within image data sets. The single-exponential fit results in a value representative of a linear combination of exponential time constants for all of the various ^{1}H environments represented in the volume element. DECRA extracts independent exponential values and renders images based upon these pure values. Tissues are not necessarily segmented in this fashion, but ^{1}H nuclear environments are. For example, the component with the shortest T_2, Fig. 2a, most likely represents predominantly the methylene signal

from the long alkyl chains in the fat and lipid tissues. The fat and muscle tissue are highlighted. T_2 values are primarily shorter for these environments because of restricted molecular mobility.

The three T_2 and two T_1 components can, as described in the theory section, represent six unique hydrogen environments. The relaxation times of these environments are summarized in Table 1. Fletcher *et al.* (2) have established ranges for the monoexponential constants for the six tissues in our imaged slice and have segmented these tissues using these ranges. For comparison purposes, we have used their technique to calculate monoexponential T_1 and T_2 constants for the six tissues in our imaged slice. The mean values for the six tissues are also listed in Table 1. Their technique was also used to help identify the locations of the six tissues in our image slice. It is possible, using this *a priori* knowledge of the location of the six tissue types found in this slice, to determine the relative amounts of the six identified hydrogen environments in the tissues. Values C_1–C_5 for *each* tissue were then found and Eqs. [6]–[10] used to determine the approximate fraction of $\rho_{i,j}$ in each tissue. The $\rho_{i,j}$ values for CSF, white, gray, meninges, adipose, and muscle tissues are presented in Table 1.

CSF consists of one unique hydrogen spin environment with $T_1 = 7.0$ s and $T_2 = 290$ ms. No other tissue type contains this type of hydrogen environment. Gray matter is surrounded by and in direct contact with this type of hydrogen environment, but gray matter itself is not composed of this type of hydrogen environment. Gray matter is composed of an approximately equal amounts of two environments: $T_1 = 7.0$ s, $T_2 = 64$ ms; and $T_1 = 0.92$ s, $T_2 = 64$ ms. White matter is composed of approximately 70% $T_1 = 0.92$ s, $T_2 = 64$ ms, and 30% $T_1 = 0.92$ s, $T_2 = 290$ ms hydrogen environments.

Meninges were composed of approximately 45% $T_1 = 0.92$ s, $T_2 = 22$ ms, 40% $T_1 = 0.92$ s, $T_2 = 64$ ms, and 15% $T_1 = 0.92$ s, $T_2 = 290$ ms environments. Adipose tissue also con-
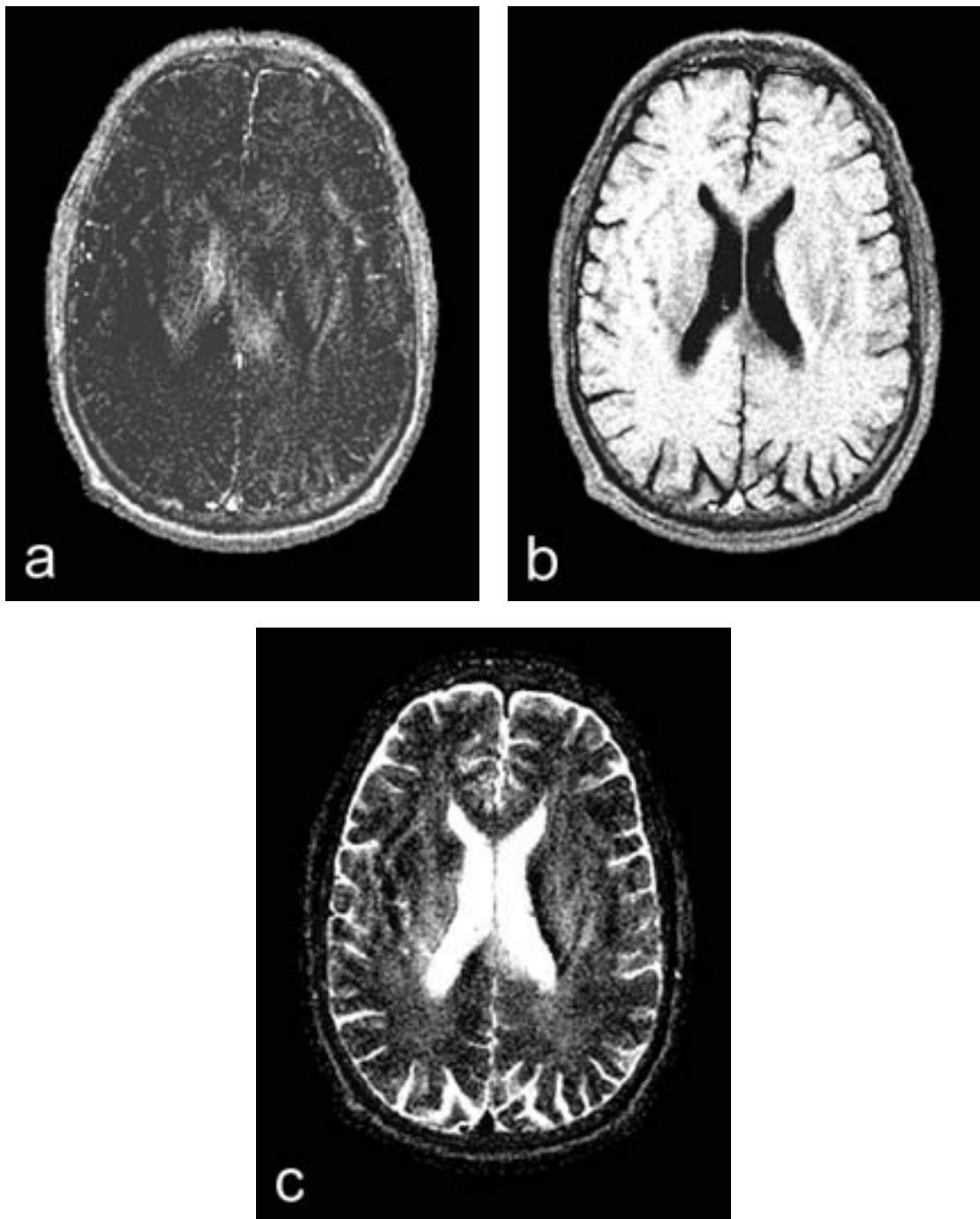
FIG. 7. Resolved images from DECRA analysis applied to T_2 image series using only images 1, 4, 7, 10, 13. Component (a) C_1, $T_2 = 16$ ms; (b) C_2, $T_2 = 63$ ms; and (c) C_3, $T_2 = 260$ ms.

tained three environments: 45% $T_1 = 0.92$ s, $T_2 = 22$ ms, 35% $T_1 = 0.92$ s, $T_2 = 64$ ms, and 20% $T_1 = 0.92$ s, $T_2 = 290$ ms. Muscle tissue contained four environments: 35% $T_1 = 0.92$ s, $T_2 = 22$ ms, 15% $T_1 = 0.92$ s, $T_2 = 64$ ms, 45% $T_1 = 7.0$ s, $T_2 = 22$ ms, and 5% $T_1 = 7.0$ s, $T_2 = 64$ ms. The uncertainty in the composition of the muscle, meninges, and adipose tissue environments is greater than that of the CSF, gray matter, and white matter because of the smaller amounts of these tissues and chemical shift artifacts in the thin closely spaced layers of adipose and muscle tissues outside of the skull.

A major advantage of DECRA is that it is a multivariate method; in other words, it uses all the pixels simultaneously. Therefore, in principle, only a few images are required for the analysis. Figure 7 shows the results of DECRA applied to images 1, 4, 7, 10, 13 of the T_2 image set. The results are very comparable with those resulting from the analysis of all 14 images. Although five single-echo images were used to calculate these eigen images, a single multiecho sequence might be used, thus reducing image acquisition time.

CONCLUSIONS

We have demonstrated the use of an algorithm based upon three-way mode analysis that, when applied to a multivariate image data set, successfully separates components which are directly related to pure and unique exponential constants. These resolved components represent the primary components within the data. The use of single exponentials resulted in a model that reconstructs the original data almost exactly. Deviations from this model, such as profiles of multiexponential character, are within the noise level and as a consequence cannot be distinguished from a model described by single exponentials. This approach has several advantages. It is fast. A full image data set composed of 15 256 $\times$ 256 pixel images can be processed in 40 s using MATLAB running on a 90-MHz, Pentium processor–based computer. The algorithm arrives at a solution directly; no iterative exponential fitting is performed. Although all 15 images were used in this study, very good results were obtained by analyzing only five images. The advantage here is that only a small number of images are needed for the analysis, depending upon the number of components present. DECRA in principle may be applied to any data set that is correlated with an exponential function. Therefore, it may be used to resolve components based upon diffusivity, T_2^*, or dynamic contrast.

Applying this algorithm to magnetic resonance images of the brain revealed six unique hydrogen environments. The environments are present in the six physiological tissues types to various extents. DECRA holds several important implications for MRI image analysis. This may be useful, for example, in quantifying pathology such as edema from a stroke occurrence. Monitoring the image representative of free water would help follow the progress of the pathology and/or treatment. Future efforts in our labs will focus on using DECRA to elucidate the exact concentrations of the hydrogen components in brain and other tissues of the human body.

REFERENCES

1. D. D. Stark and W. G. Bradley, ''Magnetic Resonance Imaging,'' 2nd Ed., Mosby, St. Louis (1992).

2. L. M. Fletcher, J. B. Barsotti, and J. P. Hornak, *Magn. Reson. Med.* **29,** 623–630 (1993).

3. J. Ma, F. W. Wehrli, H. K. Song, and S. N. Hwang, *J. Magn. Reson.* **125,** 92–101 (1997).

4. R. J. Ordidge, J. Gorell, J. Deniau, R. A. Knight, and J. A. Helpern, *Magn. Reson. Med.* **32,** 335 (1994).

5. M. Just and M. Thlen, *Radiology* **169,** 779–785 (1988).

6. Y.-H. Kao, J. A. Sorenson, M. M. Bahn, and S. S. Winkler, *Magn. Reson. Med.* **32,** 342–357 (1994).

7. J-P. Armsach, D. Gounot, L. Rumbach, and J. Chambron, *Magn. Reson. Imag.* **9,** 107–113 (1991).

8. R. M. Kroeker and R. M. Henkelman, *J. Magn. Reson.* **69,** 218–238 (1986).

9. A. E. English, M. L. G. Joy, and R. M. Henkelman, *Magn. Reson. Med.* **21,** 264–281 (1991).

10. H. Peemoeller, M. M. Pintar, and D. W. Kydon, *Biophys. J.* **29,** 427 (1980).

11. E. A. Guggenhem, *Phil. Mag.* [7] **2,** 538–543 (1926).

12. J. R. Wolberg, ''Prediction Analysis,'' Van Nostrand, Princeton, NJ (1967).

13. J. Gong and J. P. Hornak, *Magn. Reson. Imaging* **10,** 623–626 (1992).

14. X. Li and J. P. Hornak, *J. Imaging Sci. Tech.* **38,** 154–157 (1994).

15. K. P. Whittall, M. J. Bronskill, and R. M. Henkelman, *J. Magn. Reson.* **95,** 221–234 (1991).

16. H. Grahn, N. M. Szeverenyi, M. W. Roggenbuck, F. Delaglio, and P. Geladi, *Chemom. Intell. Lab. Syst.* **5,** 209–220 (1989).

17. H. Grahn, N. M. Szeverenyi, M. W. Roggenbuck, F. Delaglio, and P. Geladi, *Chemom. Intell. Lab. Syst.* **5,** 311–322 (1989).

18. H. Grahn, N. M. Szeverenyi, M. W. Roggenbuck, and P. Geladi, *Chemom. Intell. Lab. Syst.* **7,** 87–93 (1989).

19. H. F. Grahn and J. Sääf, *Chemom. Intell. Lab. Syst.* **14,** 391–396 (1992).

20. M. Kubista, *Chemom. Intell. Lab. Syst.* **7,** 273–279 (1990).

21. I. Scarminio and M. Kubista, *Anal. Chem.* **65,** 409–416 (1993).

22. K. S. Booksh and B. R. Kowalski, *J. Chemom.* **8,** 287–292 (1994).

23. D. Schulze and P. Stilbs, *J. Magn. Reson. Ser. A* **105,** 54–58 (1993).

24. B. Antalek and W. Windig, *J. Am. Chem. Soc.* **118,** 10,331–10,332 (1996).

25. W. Windig and B. Antalek, *Chemom. Intell. Lab. Syst.* **37,** 241–254 (1997).

26. W. Windig, J. P. Hornak, and B. Antalek, *J. Magn. Reson.* **132,** 298–306 (1998).